Intrinsic Focusing of the Particle Size Distribution in Colloids Containing Nanocrystals of Two Different Crystal Phases

Benjamin Voss and Markus Haase*

Department of Inorganic Chemistry I-Materials Research, Institute of Chemistry, University of Osnabrueck, Barbarastrasse 7, 49076 Osnabrueck, Germany

ABSTRACT

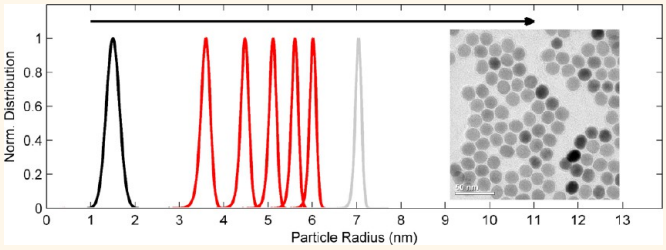

We have studied the Ostwald ripening of colloids containing nanocrystals of two different crystal phases of the same material. Ostwald ripening in such polymorphic systems is shown to result in an intrinsic focusing of the particle size distribution of the thermodynamically preferred phase while the particles of the less stable phase completely dissolve. Experimentally, a colloidal system of this kind was realized by mixing small $NaEuF_4$ nanocrystals of the cubic α-phase with particles of the hexagonal β-phase having the same mean size and size distribution. The temporal evolution of the particle sizes of both phases can be understood and numerically simulated within the framework of LSW theory. The simulations show that small differences in the bulk solubility or the surface energy of the two phases are sufficient to explain the experimentally observed narrowing of the particle size distribution.

KEYWORDS: nanoparticle growth · upconversion · Ostwald ripening · Ostwald's step rule

The use of nanocrystals in biological imaging,[1−3] solar energy conversion,[4−7] light-emitting devices,[8−10] and other applications requires the synthesis of particles with accurately defined sizes and narrow particle size distributions. In a typical nanoparticle synthesis, a large number of nuclei crystallize at early stages of the synthesis from "monomers" which are rapidly released, for instance, by the thermal decomposition of a precursor swiftly injected into the hot solution ("burst nucleation").[11−21] The nuclei subsequently grow by consuming remaining monomers in solution, thereby further decreasing the monomer concentration.[22] At sufficiently low monomer concentration, the smaller particles of the size distribution start to release monomers into the solution provided that the particles consist of a material which is at least slightly soluble in the solvent. The larger particles consume the released monomers and thereby increase in size, whereas the smaller particles decrease in size and finally dissolve completely. Under these conditions, the concentration of monomers ultimately becomes quasi-stationary; that is, the concentration decreases only very slowly with time, asymptotically approaching the equilibrium value observed over a precipitate of the bulk solid. This growth stage called Ostwald ripening[23] can be mathematically described within the framework of LSW theory named after Lifshitz, Slyozov, and Wagner.[24,25] Ostwald ripening results in a broad particle size distribution containing a small fraction of particles which are close to complete dissolution. Since the size distribution always extends to particle size 0 while the mean particle size constantly increases during Ostwald ripening, the polydispersity of the sample also increases with time.

* Address correspondence to markus.haase@uni-osnabrueck.de.

Received for review September 26, 2013 and accepted November 9, 2013.

Published online November 09, 2013
10.1021/nn405026w

Ostwald ripening can be avoided if a high concentration of monomers can somehow be maintained in solution (supersaturation of monomers). Wey and Strong[26] experimentally observed a narrowing of the particle size distribution when new monomers were added to a suspension of micrometer-sized (0.1−0.9 μm) AgBr crystals. Sugimoto[27] has shown theoretically that in the case of supersaturation of monomers and a diffusion-limited reaction between monomer and the particle surface smaller particles grow faster than larger ones resulting in a narrowing of the size distribution. Peng *et al.*[21] could convincingly show for CdSe and InAs nanocrystals that narrowing ("focusing") of the nanoparticle size distribution takes place upon injection of additional monomer precursor during growth. Sugimoto also discussed methods for keeping the monomer concentration high without the risk of exceeding the critical monomer concentration where nucleation of new particles begins. One option is the addition of a substance that can serve as a homogeneously dispersed reservoir of monomers in solution, that is, a precursor that releases monomers with a rate appropriate to maintain supersaturation conditions. While some experimental examples are already mentioned in the work by Sugimoto, only recently in-depth studies on the kinetics of precursor conversion to monomers have been performed for colloidal nanomaterials.[19,28−33] Clarke *et al.*[34] were able to derive an analytical expression for the degree of size focusing expected for a given production rate of monomers in the solution. They also compared their theoretical results with experimental data of CdSe nanocrystals and found very good agreement. Dagtepe *et al.*[35] have theoretically investigated the Ostwald ripening of bimodal size distributions, that is, the special case where the monomer precursor consists of very small particles of the same material as the growing nanocrystals. If the two particle fractions of the bimodal distribution are sufficiently well-separated in size, the dissolution rate of the smaller particles is high enough to achieve supersaturation conditions for the larger particles and a narrow size distribution is obtained. Experimentally, this method has recently been used to grow the shell of core−shell particles.[36]

Another interesting case are nanomaterials which crystallize in two or more different polymorphs. Well-known examples, among many others, are TiO_2 and several II−VI semiconductors. CdSe and CdS, for instance, can be prepared either in the cubic zinc blende phase[37,38] or in the hexagonal wurtzite phase,[17] whereas TiO_2 nanocrystals have been synthesized in the anatase[40] as well as in the rutile structure.[39] Depending on the synthesis conditions, polymorphic materials can follow Ostwald's step rule[40] stating that not the most stable but the least stable polymorph crystallizes first. This behavior has recently been discussed for II−VI quantum dots like CdSe.[37]

Another class of nanomaterials forming two different polymorphs are $NaREF_4$ nanocrystals (RE = rare earth), which can crystallize either in the cubic α-phase or in the hexagonal β-phase. Currently, nanoparticles of these materials are being thoroughly investigated owing to the distinct optical and magnetic properties of many rare-earth ions and the low phonon energies of the crystal lattices.[41−46] For several rare-earth ions, the oleic-acid-based synthesis of the $NaREF_4$ nanoparticles can be controlled in such a way that small nanocrystals of the less stable cubic α-phase are formed at early stages of the synthesis which subsequently convert to particles of the thermodynamically most stable β-phase.[47−52] The procedure yields very narrow particle size distributions without the injection of additional monomer or monomer precursor during the synthesis. Recent work has shown that the particles nevertheless grow by the exchange of monomers.[53−59] This indicates that Ostwald ripening of a colloid containing two polymorphs of the same nanomaterial can lead to an intrinsic focusing of the particle size distribution. We have therefore studied the Ostwald ripening of such binary systems both experimentally for the case of $NaEuF_4$ nanocrystals and theoretically within the framework of LSW theory. The results show that narrow particle size distributions can be achieved even if both phases display the same initial particle size distribution and no molecular precursors are added.

RESULTS AND DISCUSSION

Small nanoparticles (precursor particles) of the cubic α-phase (Figure 1a) and the hexagonal β-phase (Figure 1d) were prepared separately as starting materials for the synthesis of monodispersed β-$NaEuF_4$ nanocrystals. $NaEuF_4$ was chosen because small particles with narrow size distribution can be prepared in the hexagonal β-phase as well as in the cubic α-phase.[56] The small nanoparticles were washed several times after synthesis before they were redispersed in blank oleic acid/octadecene solvent. Heating of the resulting colloidal solutions to 320 °C results in Ostwald ripening of the particles as shown earlier by TEM investigations, EPR measurements, and luminescence spectroscopy.[36,47,54−56] If pure α-phase precursor particles are heated, the particles grow to about 12 nm before the first nanocrystals of the thermodynamically more stable β-phase can be observed in solution. In the presence of these particles, rapid dissolution of the α-phase particles occurs accompanied by fast growth of the β-phase particles. The final product consists of β-phase nanocrystals with very narrow particle size distribution.[56]

The TEM images in Figure 1 show that nearly monodispersed nanocrystals of the β-phase are also obtained when mixtures of α-phase and β-phase precursor particles are heated in oleic acid/octadecene solvent. The final particle size of the β-phase product

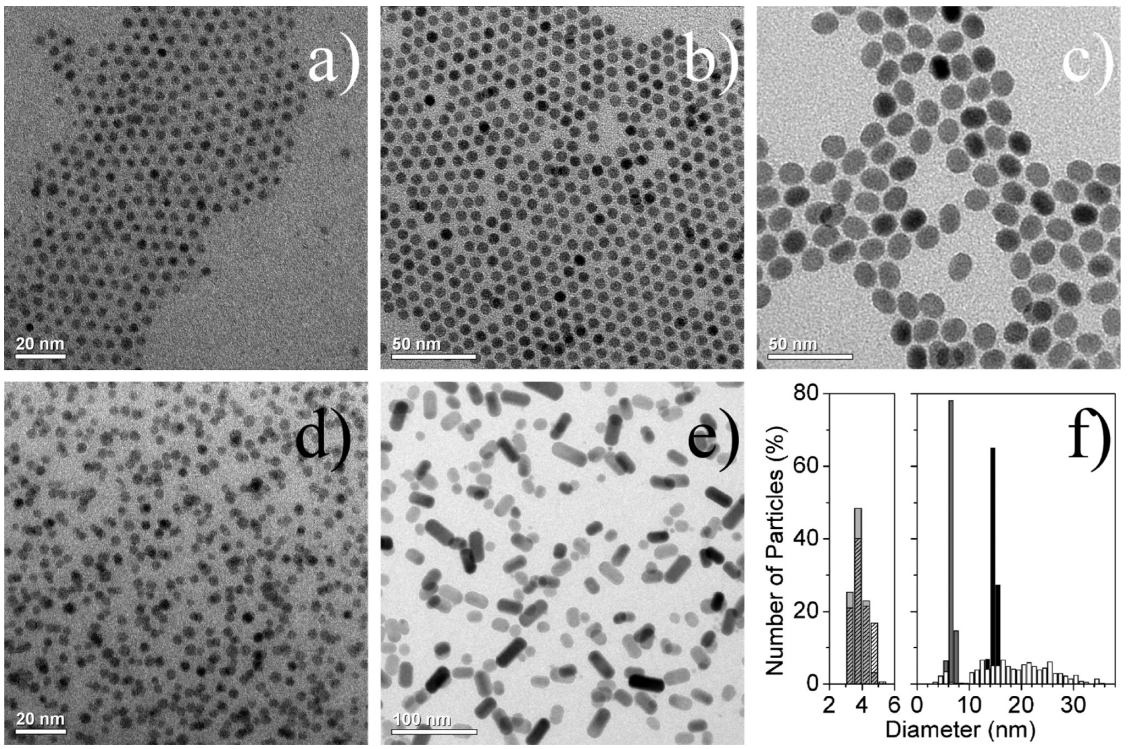

Figure 1. TEM images of $NaEuF_4$ nanocrystals. (a) Cubic phase starting material (α-phase precursor particles), (b) product particles (β-$NaEuF_4$) obtained from a 9:1 mixture of α-phase and β-phase precursor particles, (c) product particles (β-$NaEuF_4$) obtained from a 99:1 mixture of α-phase and β-phase precursor particles, (d) hexagonal phase starting material (β-phase precursor particles), (e) product particles (β-$NaEuF_4$) obtained from pure β-phase precursor particles. (f) Histograms of the particle size distribution as derived from the TEM images. Left: (a) (gray) and (d) (light gray). Right: (b) (gray), (c) (black), and (e) (light gray).

depends on the ratio of α-phase and β-phase precursor particles employed. Figure 1b,c displays the product particles obtained after heating a 9:1 and 99:1 mixture at 320 °C for 15 and 25 min, respectively. The corresponding X-ray powder diffraction data (see Supporting Information) show that both samples consist of pure β-phase material. The consumption of the α-phase material is therefore significantly faster than in our previous work where β-phase particles were not initially present in the colloidal solution.[56] This indicates that the monomers released by the α-phase have now already been consumed by the β-phase particles initially present in the mixture and not by β-phase particles which form newly after prolonged Ostwald ripening of the α-phase (as in our previous work).

For comparison, the size distribution resulting when β-phase precursor particles are heated alone is also given in Figure 1e. Only in this case, the particle growth results in the broad size distribution expected for Ostwald ripening (Figure 1f). The histograms in Figure 1f show that the standard deviation of the particle diameter increases from $\sigma = \pm 0.4$ nm for the precursor particles to $\sigma = \pm 0.45$ nm and $\sigma = \pm 0.6$ nm for the product particles in Figure 1b,c, respectively, whereas the $\sigma/\langle r \rangle$ values decrease from 10 to 7 and 3%.

The use of small particles as starting material has the advantage that the final product is solely formed by growth processes. This greatly simplifies the theoretical description of the temporal evolution of the particle size distributions because the nucleation of particles needs not to be taken into account. In order to numerically calculate the Ostwald ripening behavior of our colloidal mixtures of two polymorphs within the framework of LSW theory, we started from an expression developed by Talapin *et al.* to treat the Ostwald ripening of particles with very small size. According to Talapin *et al.*, the growth rate of a particle with radius r' is given by[60]

$$\frac{dr'}{dt'} = V_m D c_\infty^{eq} \left\{ \frac{\frac{c}{c_\infty^{eq}} - \exp\left[\frac{2\gamma V_m}{r'RT}\right]}{r' + \frac{D}{k_\infty} \exp\left[\alpha \frac{2\gamma V_m}{r'RT}\right]} \right\} \quad (1)$$

where V_m, γ, and c_∞^{eq} are the molar volume, the surface tension, and the solubility of the bulk solid ($r' \rightarrow \infty$), respectively; c is the monomer concentration in (the bulk of the) solution, D is the diffusion coefficient of the monomer, k_∞ is the (first-order) rate constant for the growth reaction between monomer and bulk solid, α is the transfer coefficient, T is the absolute temperature, and R is the gas constant. Similar to LSW theory, the derivation of eq 1 is based on the Gibbs–Thomson equation but remains valid for nanocrystals of small size because the Gibbs–Thomson equation is not

TABLE 1. Values of the Parameters Used in the Numerical Calculation of Diffusion-Limited or Reaction-Limited Ostwald Ripening

parameter		symbol	value
diffusion coefficient of monomer		D	10^{-10} m^2/s
type of reaction control		K	10^{-5} or 10^{5}
transfer coefficient		α	0.5
unit volume (colloidal solution)		V_{sol}	10^{-12} L
temperature		T	593 K
initial monomer supersaturation		S_0	0
		α-phase	**β-phase**
molar volume of solid	V_m	0.048 L/mol	0.046 L/mol
initial mean particle radius	$\langle r_0 \rangle$	1.5 nm	1.5 nm
initial standard deviation of the particle size distribution	$\sigma_0/\langle r_0 \rangle$	10%	10%

developed into a Taylor series and truncated after the linear term. When the latter approximation is applied to the exponential terms in eq 1, however, the corresponding growth law of the LSW theory is obtained[60] (see also Supporting Information for details).

Since our colloids contain two polymorphs of the same material, we used two expressions analogous to eq 1, one for the growth rate of the α-phase particle with radius $r' = r'_\alpha$, molar volume $V = V_\alpha$, surface tension $\gamma = \gamma_\alpha$, and bulk solubility ${}^{\infty}c_\alpha^{eq}$ and the second for the growth rate of the β-phase particles with radius $r' = r'_\beta$, molar volume $V = V_\beta$, surface tension $\gamma = \gamma_\beta$, and bulk solubility ${}^{\infty}c_\beta^{eq}$. To simplify the two expressions, we first define, analogous to ref 60, the capillary length L and the parameters τ and K by

$$L = \frac{2\gamma_\alpha V_\alpha^m}{RT} \qquad \tau = \frac{4\gamma_\alpha^2 V_\alpha^m}{R^2T^2D\,{}^{\infty}c_\alpha^{eq}} \qquad K = \frac{1}{L}\left(\frac{D}{k_\infty}\right) \tag{2}$$

The dimensionless parameter K defines the type of reaction control, that is, $K \to 0$ for a purely diffusion-limited reaction between the monomers and the particles and $K \to \infty$ for a purely reaction-limited process. The parameter τ has the dimension of time. Note that L, τ, and K are chosen to depend on material constants of the α-phase only. For simplicity, the rate constant k_∞ is assumed to be independent of the crystal phase. We now introduce the dimensionless radii r_α and r_β for α-phase and β-phase particles, respectively, and the dimensionless time t by

$$r_\alpha = \frac{1}{L}r'_\alpha \qquad r_\beta = \frac{1}{L}r'_\beta \qquad t = \frac{1}{\tau}t' \tag{3}$$

Furthermore, the supersaturation S of monomer in solution is defined by $S = c/c_\infty^{eq}$. Since the α-phase and the β-phase of a bulk solid will in general have different solubility c_∞^{eq}, the same monomer concentration c in solution leads to different supersaturation conditions for the two phases. The supersaturation of monomer with respect to the α- and the β-phase is therefore given by

$$S_\alpha = \frac{c}{{}^{\infty}c_\alpha^{eq}} \qquad S_\beta = \frac{c}{{}^{\infty}c_\beta^{eq}} \tag{4}$$

where ${}^{\infty}c_\alpha^{eq}$ and ${}^{\infty}c_\beta^{eq}$ are the bulk solubility of the α-phase and the β-phase, respectively. Inserting expressions 2, 3, and 4 into eq 1 yields the following expressions for the growth rate of one particle of the α-phase and the β-phase

$$\frac{dr_\alpha}{dt} = \frac{S_\alpha - \exp\left(\frac{1}{r_\alpha}\right)}{r_\alpha + K\exp\left(\frac{\alpha}{r_\alpha}\right)} \tag{5a}$$

$$\frac{dr_\beta}{dt} = \mu\frac{S_\beta - \exp\left(\frac{\eta}{r_\beta}\right)}{r_\beta + K\exp\left(\frac{\eta\alpha}{r_\beta}\right)} \tag{5b}$$

where

$$\eta = \frac{\gamma_\beta V_\beta^m}{\gamma_\alpha V_\alpha^m} \qquad \mu = \frac{{}^{\infty}c_\beta^{eq}V_\beta^m}{{}^{\infty}c_\alpha^{eq}V_\alpha^m} \qquad S_\beta = \frac{{}^{\infty}c_\alpha^{eq}}{{}^{\infty}c_\beta^{eq}}S_\alpha$$

Note that the difference of the two growth rates is mainly determined by ratios of the materials parameters, that is, the ratio of the bulk solubilities ${}^{\infty}c_\beta^{eq}/{}^{\infty}c_\alpha^{eq}$, the ratio of the surface energies $\gamma_\beta/\gamma_\alpha$, and the ratio of the densities or molar volumes $\rho_\beta/\rho_\alpha = V_\beta^m/V_\alpha^m$. The latter ratio can be expected to be very close to 1 because the densities of two phases of the same material usually differ only by a few percent. For the cubic α-phase (ICSD no. 77100) and the hexagonal β-phase (ICSD no. 51916) of $NaYF_4$, for instance, the value is $V_\beta^m/V_\alpha^m = 0.95$.

The values for the bulk solubilities and the surface tensions had to be estimated because no reliable data exist for the two phases of $NaEuF_4$ in octadecene/oleic acid solvent at 320 °C. We have chosen values similar to those for CaF_2 in water (*i.e.*, ${}^{\infty}c^{eq} = 0.2$ mmol/L and $\gamma = 0.15$ J/m^2) as given in Table 1.[61,62] Values for the mean particle size and the standard deviation of the initial size distributions were deduced from the TEM images (Figure 1) and were found to be similar in the case of α- and β-phase precursor particles. For simplicity, we therefore assumed the same Gaussian shape for the initial size distribution of both phases (Table 1). The value of the diffusion coefficient was assumed to be $D = 10^{-10}$ m^2/s, in accord with the Stokes–Einstein relation.[63]

The temporal evolution of the size distribution (*i.e.*, the distribution of particle radii) was now evaluated for both phases by numerical integration of the growth rates of all particle sizes within each distribution. The numerical procedure is based on the population balance method and the Runge–Kutta fourth-order algorithm, as already employed by other groups for the numerical simulation of nanoparticle growth.[64,65]

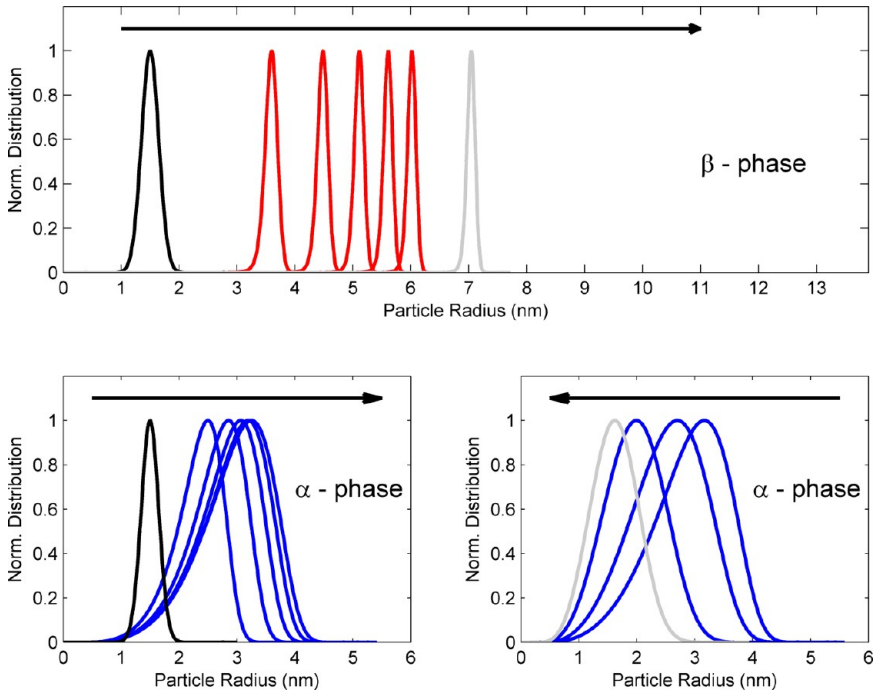

Figure 2. Numerical simulation of the evolution of the particle size distributions for a 99:1 mixture of α-phase and β-phase precursor particles (diffusion-limited case, $^{\infty}c_{\alpha}^{eq}$ = 0.2 mol/m^3, $^{\infty}c_{\beta}^{eq}$ = 0.1 mol/m^3, and $\gamma_\alpha = \gamma_\beta$ = 0.15 J/m^2). Top: Evolution of the β-phase particles (growth stages 2 and 3). Bottom: Evolution of the α-phase particles during growth stage 2 (left) and growth stage 3 (right). For both phases, changes occurring during the first growth stage are within the line width of the first particle size distribution. The arrows indicate the course of time. All distribution curves are normalized in height. Initial distribution curves (t = 0) are given in black. Gray distribution curves correspond to the last size distribution of growth stage 3 before the α-phase completely dissolves.

Since the Ostwald ripening of colloids containing nanoparticles of only one phase has already been treated in the literature, the numerical results for the growth of β-phase particles in the absence of α-phase particles (as given in the TEM images in Figure 1d,e) are only given in the Supporting Information for comparison. We have used these results, however, to verify that our algorithm for the numerical integration works flawlessly.

Since the value of the rate constant k_∞ is not known, we calculated the temporal evolution of the size distributions for purely diffusion-limited conditions and purely reaction-limited conditions as the two limiting cases. Figure 2 displays the results for the diffusion-limited case (K = 0.00001) and a colloid initially containing α-phase and β-phase particles in a mass ratio of 99:1. The bulk solubility of the two phases is assumed to be slightly different ($^{\infty}c_{\alpha}^{eq}$ = 0.2 mmol/L, $^{\infty}c_{\beta}^{eq}$ = 0.1 mmol/L), whereas the surface tension is assumed to be the same ($\gamma_\alpha = \gamma_\beta$ = 0.15 J/m^2). The upper part of the figure displays the temporal evolution of the β-phase particles showing a strong narrowing of the size distribution. In contrast to the β-phase, the evolution of the α-phase is characterized by a broadening of the particle size distribution. The particles first grow in size (left-hand side of the figure) and then decrease in size before they completely dissolve (right-hand side of the figure). Note that all distribution curves have been normalized in height. Without normalization, the height of the curves in the lower part of the image rapidly decreases with time due to the decreasing number of α-phase particles in the system (see below).

The different growth stages are easier to distinguish by comparing the temporal evolution of the mean particle size of each phase with the so-called critical radius. The critical radius defines the particle size with growth rate 0, that is, the particle size being in equilibrium with the monomer concentration in solution. Particles with radius smaller than the critical radius release monomers into solution and decrease in size, whereas particles with a radius larger than the critical radius grow by consuming monomers. Setting the growth rates given by eqs 5a and 5b equal to 0 yields the following expressions for the dimensionless critical radius of the α-phase and the β-phase

$$r_\alpha^{cr} = \frac{1}{\ln(S_\alpha)} \qquad r_\beta^{cr} = \frac{\eta}{\ln(S_\beta)} \tag{6}$$

Note that supersaturation values S_α or S_β of less than 1 are obtained for monomer concentrations lower than $^{\infty}c_{\alpha}^{eq}$ or $^{\infty}c_{\beta}^{eq}$, respectively (eq 4). If the concentration of monomers is that small, all particle sizes including the bulk solid will release monomers into the solution. In this case, no particle size is in equilibrium with the monomer, and therefore, no critical radius exists. Equation 6 is therefore only valid for supersaturation values

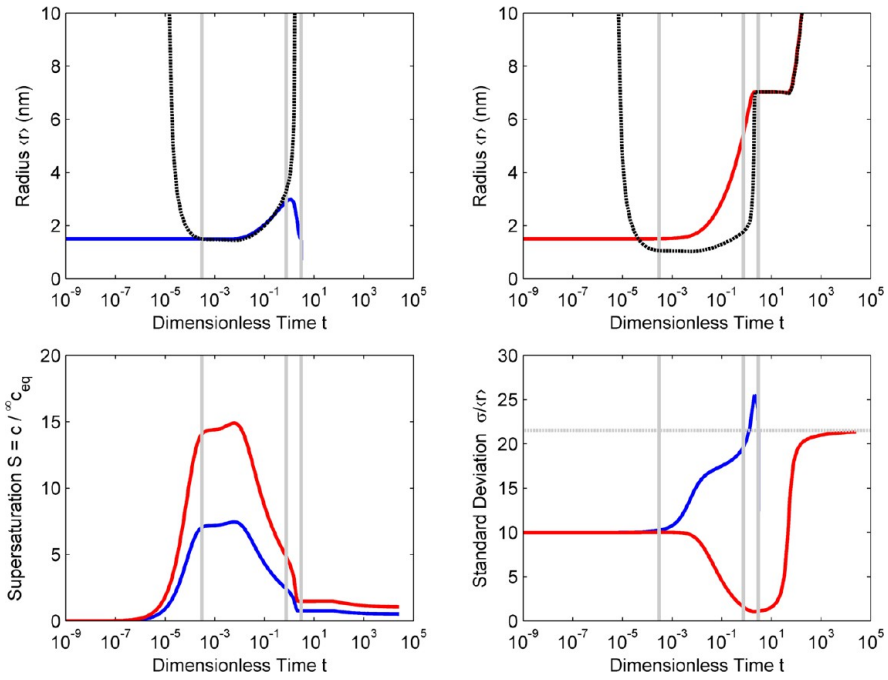

Figure 3. Numerical simulation of the temporal evolution of a 99:1 mixture of α-phase and β-phase precursor particles (diffusion-limited case, $^{\infty}c_{\alpha}^{eq}$ = 0.2 mol/m^3, $^{\infty}c_{\beta}^{eq}$ = 0.1 mol/m^3, and $\gamma_{\alpha} = \gamma_{\beta}$ = 0.15 J/m^2). Top left: Mean particle radius $\langle r \rangle$ (solid line) and critical radius r_{α}^{cr} (broken line) of the α-phase. Top right: Mean particle radius $\langle r \rangle$ (solid line) and the critical radius r_{β}^{cr} (broken line) of the β-phase. Bottom left: Evolution of the monomer concentration c in solution given as supersaturation $S_{\alpha} = c/^{\infty}c_{\alpha}^{eq}$ (blue line) and supersaturation $S_{\beta} = c/^{\infty}c_{\beta}^{eq}$ (red line). Bottom right: Standard deviation $\sigma/\langle r \rangle$ of the size distribution of the α-phase (blue line) and β-phase particles (red line). Vertical lines separate the four growth stages.

larger than 1 and yields meaningless negative values if S_{α} or S_{β} is smaller than 1.

The critical radius can be used to identify four different growth stages of our colloids, as shown in Figure 3. The figure displays numerical results for the temporal evolution of the mean radius, critical radius, supersaturation, and the width of the size distribution for both phases of the 99:1 mixture under diffusion-limited conditions ($^{\infty}c_{\alpha}^{eq}$ = 0.2 mmol/L, $^{\infty}c_{\beta}^{eq}$ = 0.1 mmol/L, $\gamma_{\alpha} = \gamma_{\beta}$ = 0.15 J/m^2 as in Figure 2). The four growth stages are separated in the figure by vertical lines.

During the first stage, the precursor particles of both phases release monomers because the particles are dispersed in blank solvent containing no monomer. As long as the monomer concentration is sufficiently low, the critical radius of both phases is larger than the mean particle size (Figure 3a,b). Depending on the concentration, surface tension, and bulk solubility of the two phases, the release of monomers decreases the size of the precursor particles. In our case, the decrease in size is small because the particle concentration is high and the bulk solubility as well as the surface tension are assumed to be small. If higher values for the surface tension are used in the simulation, however, a significant fraction of the particles of both phases not only decrease in size but also dissolve completely. This is shown in the Supporting Information for the case that $\gamma_{\alpha} = \gamma_{\beta}$ = 0.5 J/m^2.

With increasing monomer concentration in solution and, hence, increasing supersaturation S_{α} and S_{β}, the critical radii r_{α}^{cr} and r_{β}^{cr} decrease and eventually enter the particle size range of each phase. At this point, the second stage of particle growth begins. Since our colloidal mixture initially contains only 1% of β-phase particles, the monomer concentration at the beginning of the second stage is mainly determined by the properties of the α-phase. Figure 3 shows that the critical radius r_{α}^{cr} approaches a value very close to the mean particle radius of the α-phase. Particles with a size below r_{α}^{cr} therefore decrease in size, whereas the larger particles consume monomers and grow. The growth behavior of the α-phase is therefore similar to Ostwald ripening of a colloid containing only particles of one phase. In contrast to classic Ostwald ripening, however, the supersaturation is not quasi-stationary, and the ratio of the mean radius and the critical radius is not exactly equal to 1 in the diffusion-limited case (or exactly equal to 8/9 in the reaction-limited case as discussed below). The growth of the α-phase particles during stage 2 may therefore be called pseudo-Ostwald ripening.

The β-phase particles behave differently because the lower bulk solubility of the β-phase results in a higher value S_{β} for the supersaturation compared to the value of S_{α}. During stage 2, the high monomer concentration caused by the high content of better soluble α-phase particles results in a supersaturation value S_{β} so high that the critical radius r_{β}^{cr} becomes smaller than the radius of all particles of the β-phase size distribution (Figure 3). Consequently, all particles of the β-phase continuously grow during the second

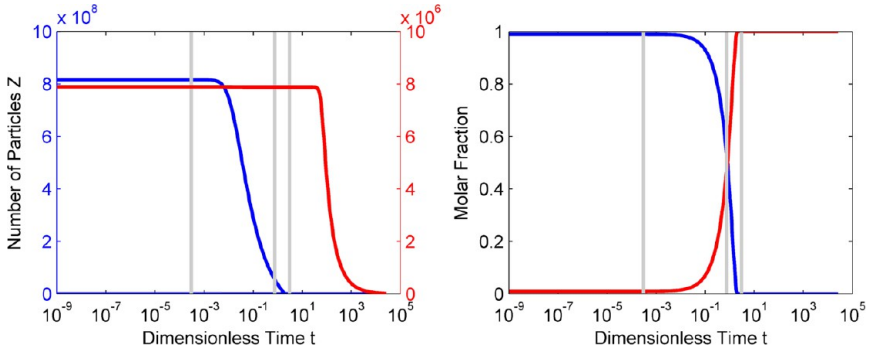

Figure 4. Numerical simulation of the temporal evolution of a 99:1 mixture of α-phase (blue lines) and β-phase precursor particles (red lines) (diffusion-limited case, $^{\infty}c_{\alpha}^{eq}$ = 0.2 mol/m^3, $^{\infty}c_{\beta}^{eq}$ = 0.1 mol/m^3, and $\gamma_\alpha = \gamma_\beta$ = 0.15 J/m^2). Evolution of the number of particles (left) and the mole fraction of the two phases (right).

growth stage. Figure 4 shows that this finally leads to an increase of the molar fraction of β-phase particles because at the same time the smaller particles of the α-phase release monomer and decrease in size. The increasing molar fraction of β-phase particles during growth stage 2 leads to a lower monomer concentration in solution because of the lower solubility of the β-phase. Moreover, the increasing size of the growing β-phase particles further decreases the release of monomers due to the Gibbs−Thomson effect. The decreasing monomer concentration results in decreasing values for S_α and S_β and increasing values for the critical radii r_α^{cr} and r_β^{cr} at the end of the second growth stage (Figure 3). Finally, the value of the critical radius r_α^{cr} becomes again larger than the largest particles of the α-phase distribution whereas the increasing value of the critical radius r_β^{cr} approaches the size range of the β-phase size distribution.

This is the beginning of growth stage 3, where all particles of the α-phase decrease in size and finally dissolve because their radii are smaller than the critical radius r_α^{cr}. The monomer thereby released is mainly consumed by the β-phase particles. Since the number of β-phase particles still remains constant, the increase of the particle size from the precursor particles to the final β-phase product is mainly determined by the initial molar ratio of the α-phase to the β-phase (compare also Figure 1a with Figure 1b,c). The latter does not change very much when the surface tension of both phases is increased to $\gamma_\alpha = \gamma_\beta$ = 0.5 J/m^2 (see above), causing 20% of the β-particles to dissolve during the first growth stage. In this case, all monomer released is consumed by the remaining 80% of β-phase particles, but this reduced number of particles increases the final particle size only by additional 8% ($0.8^{(-1/3)}$).

The narrow particle size distribution shown in Figures 2 and 3 for the β-phase is not limited to the value of $\gamma_\alpha = \gamma_\beta$ = 0.15 J/m^2 for the surface tension. Strong focusing is also observed, for instance, when the surface tension of both phases is increased to $\gamma_\alpha = \gamma_\beta$ = 0.5 J/m^2 or decreased to $\gamma_\alpha = \gamma_\beta$ = 0.05 J/m^2 (see Supporting Information for figures analogous to Figures 2 and 3).

At the end of the third growth stage, the colloid contains only β-phase particles and a low concentration of monomers. The low monomer concentration causes the critical radius r_β^{cr} of the β-phase to finally lie within the narrow particle size distribution of the β-phase (Figure 3). Heating of the reaction mixture should then be stopped because otherwise Ostwald ripening of the β-phase particles sets in, causing a broadening of the size distribution. In the numerical simulation (Figure 3), this fourth growth stage is included, displaying the characteristic features of Ostwald ripening of a colloid containing particles of one crystal phase only. In accord with LSW theory and the assumed diffusion-limited growth, the critical radius becomes identical to the mean radius and the relative standard deviation $\sigma/\langle r\rangle$ of the size distribution slowly approaches the asymptotic value of 21.5%.

Figure 3 shows that the narrow particle size distribution of the β-phase develops mainly during the second growth stage. During this stage, the β-phase particles grow under supersaturation conditions which persist for a long time due to the high content of α-phase particles in the reaction mixture. During this time, the critical radius r_β^{cr} is significantly smaller than the mean radius of the β-phase. This is the classic condition for focusing in the diffusion-limited case.[27] In fact, very strong focusing is observed in our case although the bulk solubility of the two phases is not very different ($^{\infty}c_{\alpha}^{eq}$ = 0.2 mmol/L, $^{\infty}c_{\beta}^{eq}$ = 0.1 mmol/L). The focusing is less strong but still pronounced ($\sigma/\langle r\rangle$ = 3%) for the 9:1 mixture of α-phase and β-phase particles where supersaturation conditions persist for a shorter period of time (see Supporting Information for figures analogous to Figures 2 and 3).

Narrow size distributions of the β-phase are not only obtained when the bulk solubility of the two phases is different but also when the surface tensions are not identical. When the temporal evolution of the 99:1 and the 9:1 mixture is calculated with the values γ_α = 0.25 J/m^2, γ_β = 0.15 J/m^2, and $^{\infty}c_{\alpha}^{eq} = {}^{\infty}c_{\beta}^{eq}$ = 0.1 mmol/L, for instance, almost the same small $\sigma/\langle r\rangle$ values are obtained as in the case of the different solubilities ($^{\infty}c_{\alpha}^{eq}$ = 0.2 mmol/L, $^{\infty}c_{\beta}^{eq}$ = 0.1 mmol/L, and $\gamma_\alpha = \gamma_\beta$ = 0.15 J/m^2) (see Supporting

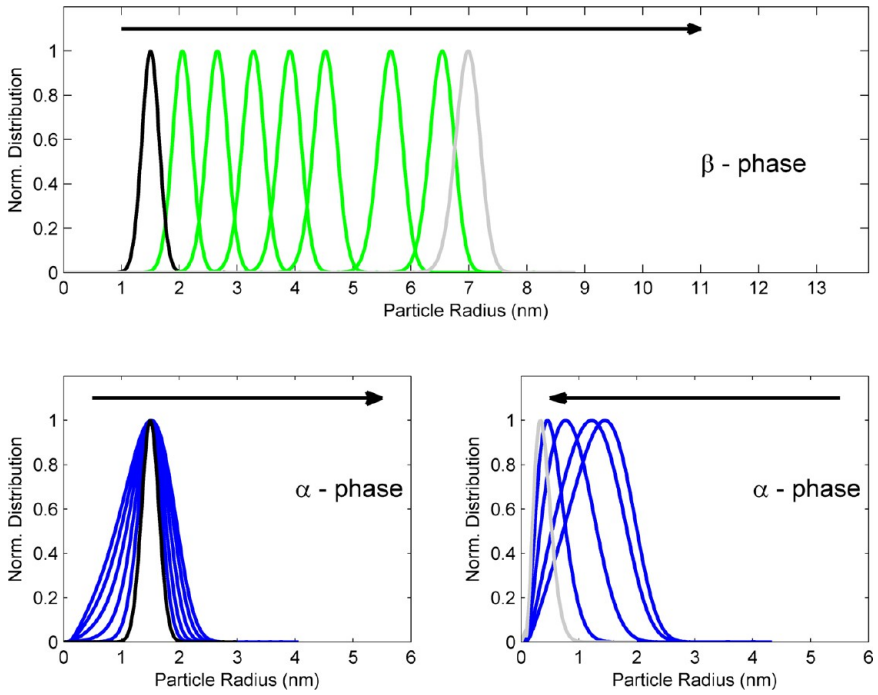

Figure 5. Numerical simulation of the evolution of the particle size distributions for a 99:1 mixture of α-phase and β-phase precursor particles (reaction-limited case, $^{\infty}c_{\alpha}^{eq}$ = 0.5 mol/m^3, $^{\infty}c_{\beta}^{eq}$ = 0.1 mol/m^3, and $\gamma_{\alpha} = \gamma_{\beta}$ = 0.05 J/m^2). Top: Evolution of the β-phase particles (growth stages 2 and 3). Bottom: Evolution of the α-phase particles during growth stage 2 (left) and growth stage 3 (right). For both phases, changes occurring during the first growth stage are within the line width of the first particle size distribution. The arrows indicate the course of time. All distribution curves are normalized in height. Initial distribution curves (t = 0) are given in black. Gray distribution curves correspond to the last size distribution of growth stage 3 before the α-phase completely dissolves.

Information for figures analogous to Figures 2 and 3). Different surface tensions also cause focusing of the final size distribution because the r_{β} values in eq 5b are all divided by the same factor η (with the exception of one r_{β} in the denominator). This factor η, however, contains the ratio of the surface tensions of the two phases (see above) and is therefore not close to 1 if the surface tensions are significantly different. In this case, the factor η increases or decreases all radii r_{β} of the β-phase in eq 5b, whereas the radii r_{α} of the α-phase in eq 5a are not affected. The consequence is that the mixture of α-phase and β-phase particles behaves mathematically like a colloid with bimodal size distribution although the real size distributions of the two phases are identical. The Ostwald ripening of bimodal size distributions, however, also leads to focusing as already shown theoretically by Chikan and Dagtepe (see introduction).[35]

While the numerical results discussed so far successfully explain the narrow particle size distribution of the product, they fail to correctly reproduce the experimentally observed reaction times. When the values summarized in Table 1 are inserted in the expression given above for the parameter τ, synthesis times of less than 1 s are the result. In principle, this problem could be solved by reducing the bulk solubilities $^{\infty}c_{\alpha}^{eq}$ and $^{\infty}c_{\beta}^{eq}$ by 3−5 orders of magnitude while keeping the ratio $^{\infty}c_{\alpha}^{eq}/^{\infty}c_{\beta}^{eq}$ constant. This would result in the same growth behavior but much larger reaction times since the parameter τ increases inversely proportionally to $^{\infty}c_{\alpha}^{eq}$ (see eq 2), whereas the growth rates of the two phases are only affected by the ratio $^{\infty}c_{\alpha}^{eq}/^{\infty}c_{\beta}^{eq}$ (see eq 5). A similar dependency on the bulk solubility $^{\infty}c^{eq}$ of the solid exists for classic Ostwald ripening of a single phase, where the growth rate of the mean radius increases proportionally to $(D\ ^{\infty}c^{eq})^{1/3}$ under diffusion-limited conditions (Wagner, equation VII.20) and proportionally to $(k\ ^{\infty}c^{eq})^{1/2}$ under reaction-limited conditions (Wagner, equation VIII.20). The assumption of bulk solubilities in the nanomolar regime, however, appears questionable. Moreover, the histograms in Figure 1f show that the standard deviation of the particle diameter increases from $\sigma = \pm 0.4$ nm for the precursor particles to $\sigma = \pm 0.6$ nm for the product particles in Figure 1c. Since the standard deviation σ does not decrease during growth, the observed particle size distributions can also result from reaction-limited particle growth. Recent work on semiconductor nanoparticles, in fact, indicates that the particles grow under reaction-limited conditions.[63,65]

We have therefore repeated the numerical calculations for the reaction-limited case (assuming K = 100 000). The numerical results for the 99:1 mixture of α-phase and β-phase precursor particles are displayed in Figures 5 and 6. The parameters used in the calculation are summarized in Table 1. The figures, which are analogous to Figures 2 and 3, show that narrow particle size distributions are obtained again when the bulk solubility of the β-phase is smaller than the bulk solubility of the α-phase. Compared to the

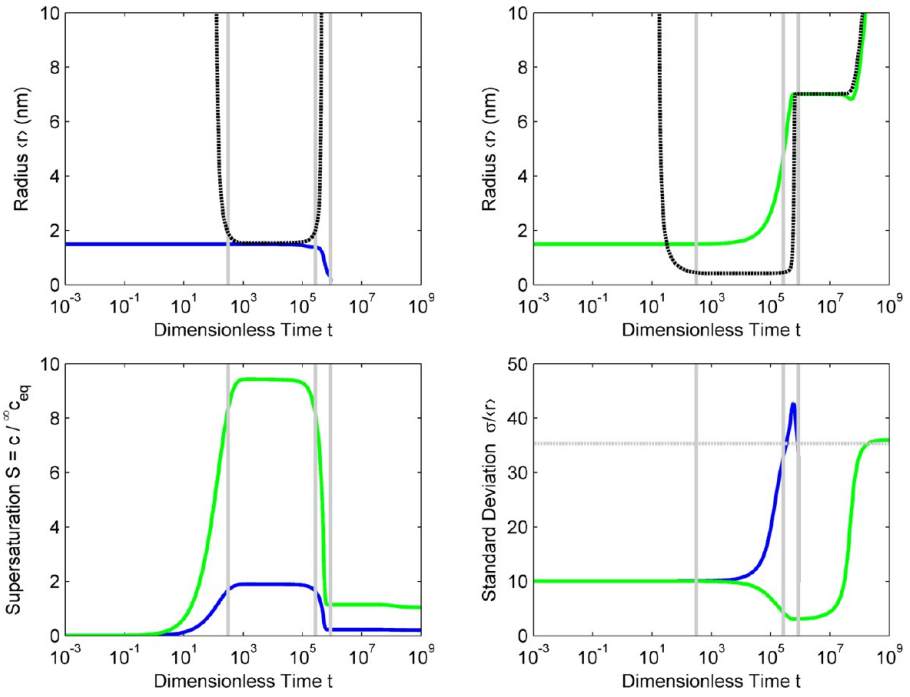

Figure 6. Numerical simulation of the evolution of the particle size distributions for a 99:1 mixture of α-phase and β-phase precursor particles (reaction-limited case, $^{\infty}c_{\alpha}^{eq}$ = 0.5 mol/m^3, $^{\infty}c_{\beta}^{eq}$ = 0.1 mol/m^3, and $\gamma_\alpha = \gamma_\beta$ = 0.05 J/m^2). Top left: Mean particle radius $\langle r\rangle$ (solid line) and critical radius r_α^{cr} (broken line) of the α-phase. Top right: Mean particle radius $\langle r\rangle$ (solid line) and the critical radius r_β^{cr} (broken line) of the β-phase. Bottom left: Evolution of the monomer concentration c in solution given as supersaturation $S_\alpha = c/^{\infty}c_{\alpha}^{eq}$ (blue line) and supersaturation $S_\beta = c/^{\infty}c_{\beta}^{eq}$ (green line). Bottom right: Standard deviation $\sigma/\langle r\rangle$ of the size distribution of the α-phase (blue line) and β-phase particles (green line). Vertical lines separate the four growth stages.

diffusion-limited case, however, the difference of the bulk solubilities has to be larger to obtain $\sigma/\langle r\rangle$ values in accord with the TEM images in Figure 1. Figure 5 shows that a $\sigma/\langle r\rangle$ value of 2.9% is obtained for the size distribution of the β-phase when values of $^{\infty}c_{\alpha}^{eq}$ = 0.5 mmol/L, $^{\infty}c_{\beta}^{eq}$ = 0.1 mmol/L, and $\gamma_\alpha = \gamma_\beta$ = 0.05 J/m^2 are used in the numerical calculation. The same values yield a $\sigma/\langle r\rangle$ value of 5.9% in the case of the 9:1 mixture (see Supporting Information for figures analogous to Figures 5 and 6). As in the diffusion-limited case, narrow size distributions of the β-phase are also obtained when the surface tensions are not identical. When the temporal evolution of the 99:1 and the 9:1 mixture is calculated with the values γ_α = 0.25 J/m^2, γ_β = 0.05 J/m^2, and $^{\infty}c_{\alpha}^{eq} = {}^{\infty}c_{\beta}^{eq}$ = 0.1 mmol/L, for instance, almost the same $\sigma/\langle r\rangle$ values as in the case of the different solubilities are obtained (see Supporting Information for figures analogous to Figures 5 and 6). The figures show that during reaction-limited growth only the $\sigma/\langle r\rangle$ value of the size distribution of the β-phase decreases but not the standard deviation σ itself. In accord with the results of LSW theory for reaction-limited Ostwald ripening, the ratio of the critical particle radius and the mean particle radius has a value of 8/9 during the fourth growth stage and the relative standard deviation $\sigma/\langle r\rangle$ of the size distribution approaches an asymptotic value of 35.3%.

The growth conditions are predominantly reaction-limited if the parameter K exceeds values of approximately K = 1000. Higher values for K only weakly affect the calculated size distributions but still have a strong influence on the calculated reaction times. The calculated reaction time can therefore be easily shifted to the experimentally observed values by choosing appropriate values for K and/or for the bulk solubilities. In the Supporting Information, two examples are given where the parameter K has been adjusted accordingly ($K = 8.8 \times 10^5$ and $K = 3.3 \times 10^5$ instead of $K = 1 \times 10^5$ for the case of different bulk solubilities and the case of different surface tensions, respectively). However, since neither the exact value of K nor the exact values of the surface tensions and bulk solubilities are known, no further attempt was made to fit the experimental data. Instead, we have investigated how different the two phases have to be in order to obtain a narrow particle size distribution of the β-phase. Thus we have systematically varied the surface tension and the bulk solubility and numerically calculated the temporal evolution for diffusion-limited and reaction-limited growth until the width of the size distribution of the β-phase had reached the minimum value (compare with Figures 3 and 6). In Figure 7, this minimum value of the relative standard deviation $\sigma/\langle r\rangle$ is plotted *versus* the ratio of the surface tension $\gamma_\alpha/\gamma_\beta$ and the ratio of the bulk solubilities $^{\infty}c_{\alpha}^{eq}/{}^{\infty}c_{\beta}^{eq}$, respectively. The figure shows again that a narrowing of the size distribution is more pronounced under diffusion-limited conditions than under reaction-limited conditions.

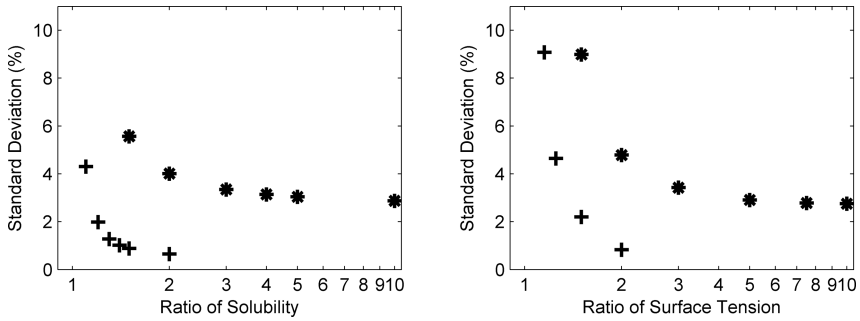

Figure 7. Influence of the material parameters of the α-phase and the β-phase on the focusing of the β-phase size distribution (numerical simulation, 99:1 mixture of α-phase and β-phase precursor particles). Displayed are the minimum values of the standard deviation $\sigma/\langle r\rangle$ obtained for different ratios of the (left) bulk solubilities, ${}^{\infty}c_{\alpha}^{eq}/{}^{\infty}c_{\beta}^{eq}$ and surface tensions, $\gamma_\alpha/\gamma_\beta$ (right), in the simulation of diffusion- (+) and reaction-limited (*) Ostwald ripening.

The figure also shows that narrowing occurs only when any of the two ratios is significantly larger than 1. For $NaEuF_4$, the latter should, in fact, be the case for the solubility ratio ${}^{\infty}c_{\alpha}^{eq}/{}^{\infty}c_{\beta}^{eq}$ because at temperatures below 800 °C the α-phase of bulk $NaEuF_4$ is known to be thermodynamically less stable than the β-phase.[66] The thermodynamic stability of bulk solids, however, is mainly determined by their lattice enthalpy. As a general rule, the solubility of solid materials decreases with increasing lattice enthalpy, provided that the enthalpy of solvation of the ions (released monomers in solution) is comparable among the materials. For two phases of the same material, the lattice enthalpies are therefore directly connected to the bulk solubilities since both phases release the same monomer material. A lower bulk solubility must therefore be expected for the β-phase due to its higher lattice enthalpy. In the case of $NaEuF_4$, the ratio of the bulk solubilities ${}^{\infty}c_{\alpha}^{eq}/{}^{\infty}c_{\beta}^{eq}$ should therefore at least not be smaller than 1.

Whether the ratio of the surface tensions $\gamma_\alpha/\gamma_\beta$ is larger than 1 or not is less clear. It is noteworthy, however, that $NaEuF_4$ and $NaGdF_4$ precursor particles of the cubic α-phase can be prepared only in the presence of a large excess of NaF.[56,67] In the absence of excess NaF, precursor particles of the hexagonal β-phase nucleate first.[43] This probably indicates that in the absence of excess NaF the surface tension of the β-phase is smaller than the surface tension of the α-phase because the activation energy for nucleation depends on the third power of the surface tension of the phase.[68] Since the Ostwald ripening of the particle mixture takes place in blank solvent, that is, in the absence of a large amount of excess NaF, our growth conditions resemble those where nucleation of β-phase particles is favored. Therefore, the ratio of the surface tensions $\gamma_\alpha/\gamma_\beta$ could, in fact, be larger than 1 in our case. Narrow size distributions are even possible, however, when the ratio of the surface tensions $\gamma_\alpha/\gamma_\beta$ is slightly smaller than 1, provided that the solubility ratio ${}^{\infty}c_{\alpha}^{eq}/{}^{\infty}c_{\beta}^{eq}$ is sufficiently large.

Finally, we note that even in the worst case of purely reaction-limited growth the difference in solubility or surface tension required to obtain narrow size distributions is within the range of experimentally observed values. In the case of titanium dioxide, for instance, the surface tension of the anatase and rutile phase is reported to differ by a factor of 5.[69] In the case of zinc sulfide, the bulk solubility of the cubic phase is approximately 8 times higher than the solubility of the hexagonal phase, as derived from a difference of 10 kJ/mol in lattice enthalpy and the Hoffman approach.[70]

CONCLUSION

In conclusion, our work shows that nanoparticles with very narrow size distribution can be synthesized by Ostwald ripening of a particle mixture containing small particles of two different crystal phases. If the bulk solubility or the surface tension of the two phases is sufficiently different, an intrinsic focusing of the particle size distribution of one phase is observed accompanied by the dissolution of the particles of the second phase. Narrow particle size distributions are not only observed in the case of diffusion-limited growth but also for reaction-limited growth. In the case of reaction-limited growth, however, the difference in solubility and/or surface tension has to be larger than in the diffusion-limited case. The numerical calculations qualitatively explain the experimentally observed narrow particle size distributions of $NaEuF_4$ nanocrystals.

METHODS

Materials. Sodium oleate, ammonium fluoride, sodium fluoride, oleic acid, and octadecene were purchased from Sigma Aldrich and Alfa Aesar and used as received. The hydrated $EuCl_3$ was purchased from Treibacher Industries AG.

Synthesis of Europium Oleate. Europium oleate was prepared according to a method given in the literature.[71] Therefore, 60 mmol hydrated $EuCl_3$ (21.9 g) was dissolved in 120 mL of ethanol and 90 mL of water. When 180 mmol of sodium oleate (54.8 g) and 210 mL hexane were added to the clear solution, a

yellowish waxy solid precipitated immediately, which dissolved in the upper organic layer during refluxing for 14 h (at approximately 60 °C). From the cold solution, the upper organic layer, containing the europium oleate, was separated. After removal of the hexane with a rotavap, europium oleate remained as a soft waxy solid.

$NaEuF_4$ Precursor Particles of the Cubic α-Phase. The α-phase precursor particles of $NaEuF_4$ were synthesized as in our previous paper.[56] A related procedure was published earlier by Liu *et al.*[67] Typically, 60 mmol europium oleate (60 g) and 480 mmol sodium fluoride (20 g) were combined with 300 mL of oleic acid and 300 mL of octadecene. The resulting turbid solution was degassed on a vacuum Schlenk line (1 mbar) for 1 h at 100 °C under vigorous stirring. Thereafter, the reaction mixture was stirred at 200 °C for 60 min under nitrogen flow. The solution remained turbid due to the excess of sparingly soluble sodium fluoride. After being cooled to room temperature, the excess sodium fluoride was removed by centrifugation. The addition of an equal volume of ethanol to the clear yellowish supernatant leads to precipitation of the precursor particles, which could be separated by centrifugation. To purify the particles, the precipitate was redispersed in 180 mL of hexane, followed again by precipitation with ethanol and separation by centrifugation. The purified precursor particles were kept in this muddy state and stored in a refrigerator.

$NaEuF_4$ Precursor Particles of the Hexagonal β-Phase. For the synthesis of hexagonal phase precursor particles, 15 mmol of europium oleate (15 g) and 37.5 mmol sodium oleate (11.5 g) were heated in 75 mL of oleic acid and 75 mL of octadecene at 100 °C for 1 h under vacuum (1 mbar) and vigorous stirring at a Schlenk line. Then, 60 mmol of solid ammonium fluoride (2.22 g) was added to the clear yellowish solution under nitrogen flow and the oxygen content further reduced by cycling the setup three times between vacuum (vacuum applied for a few seconds only) and nitrogen atmosphere. After the reaction mixture was heated at 200 °C for 60 min under nitrogen flow and vigorous stirring, a clear solution was obtained from which the nanoparticles were precipitated and purified as given above for the cubic material.

Growth of the Final Product Particles. A 100 mL three-necked flask with attached thermosensor and reflux condenser was connected to a Schlenk line. In this flask, 0.063 g of hexagonal phase and 6.342 g of cubic phase $NaEuF_4$ precursor particles were redispersed in 25 mL of oleic acid and 25 mL of octadecene by stirring at 100 °C for 60 min under vacuum. After three cycling steps between vacuum and nitrogen, the setup was heated to 320 °C under vigorous stirring with a minimum heating rate of 15 °C per minute. For monitoring the reaction, samples of 8 mL were taken from time to time and the nanoparticles precipitated with a 1:2 mixture of hexane/ethanol. The precipitates were purified as described above for the precursor particles. Each sample was investigated by TEM and XRD measurements. The amounts of precursor particles used in the synthesis correspond to a 1:99 molar ratio of hexagonal and cubic phase material. This ratio reproducibly leads to 15 nm β-$NaEuF_4$ nanoparticles. An analogous procedure employing hexagonal and cubic phase precursor particles in a molar ratio of 1:9 reduces the particle size of the β-$NaEuF_4$ product to 7 nm.

Instrumentation. Transmission electron microscopy (TEM) images were taken with a JEOL JEM 2100 transmission electron microscope using a LaB_6 cathode and an acceleration voltage of 200 kV. Size histograms of the samples were derived from TEM images using the software ImageJ.[72] For each histogram, the size of 200 to 500 particles was analyzed. Hexagonal phase $NaEuF_4$ nanocrystals often form elongated or rod-shaped particles (elongation along the crystallographic *c*-axis) like those displayed in Figure 1c,e. In these cases, the length and the width of each particle were determined from the TEM images, and the volume of each particle was calculated by assuming a cylindrical shape. The radius of a sphere with identical volume was then calculated from this value and used for the histogram. X-ray powder diffraction measurements were performed on an X'Pert Pro diffractometer (Panalytical) with Bragg–Brentano geometry using Cu Kα (λ = 1.5406 Å) radiation (40 kV, 40 mA) and a 2θ step size of 0.0334°. The instrumental resolution function was determined with Y_2O_3 powder as standard. The molar fractions of the two phases were evaluated by the Rietveld method using the Full-Prof software (version July 2011. LLB, Juan Rodriguez Carvajal, Saclay France).[73]

Conflict of Interest: The authors declare no competing financial interest.

Acknowledgment. We thank Henning Eickmeier for preparing the TEM images, and Matthias König for help with the Matlab software.

Supporting Information Available: XRD data, additional numerical calculations, as well as a brief description and tests of the simulation algorithm are given. This material is available free of charge *via* the Internet at http://pubs.acs.org.

REFERENCES AND NOTES

1. Wang, Y.; Hu, R.; Lin, G.; Roy, I.; Yong, K.-T. Functionalized Quantum Dots for Biosensing and Bioimaging and Concerns on Toxicity. *ACS Appl. Mater. Interfaces* **2013**, *5*, 2786–2799.
2. Bouzigues, C.; Gacoin, T.; Alexandrou, A. Biological Applications of Rare-Earth Based Nanoparticles. *ACS Nano* **2011**, *5*, 8488–8505.
3. Medintz, I. L.; Uyeda, H. T.; Goldman, E. R.; Mattoussi, H. Quantum Dot Bioconjugates for Imaging, Labelling and Sensing. *Nat. Mater.* **2005**, *4*, 435–446.
4. Chan, E. M.; Gargas, D. J.; Schuck, P. J.; Milliron, D. J. Concentrating and Recycling Energy in Lanthanide Codopants for Efficient and Spectrally Pure Emission: The Case of $NaYF_4$: Er^{3+}/Tm^{3+} Upconverting Nanocrystals. *J. Phys. Chem. B* **2012**, *116*, 10561–10570.
5. Shalav, A.; Richards, B. S.; Trupke, T.; Krämer, K. W.; Güdel, H. U. Application of $NaYF_4$:Er^{3+} Up-converting Phosphors for Enhanced Near-Infrared Silicon Solar Cell Response. *Appl. Phys. Lett.* **2005**, *86*, 013505.
6. Shan, G.-B.; Assaaoudi, H.; Demopoulos, G. P. Enhanced Performance of Dye-Sensitized Solar Cells by Utilization of an External, Bifunctional Layer Consisting of Uniform β-$NaYF_4$:Er^{3+}/Yb^{3+} Nanoplatelets. *ACS Appl. Mater. Interfaces* **2011**, *3*, 3239–3243.
7. Zhang, Q.; Uchaker, E.; Candelaria, S. L.; Cao, G. Nanomaterials for Energy Conversion and Storage. *Chem. Soc. Rev.* **2013**, *42*, 3127–3171.
8. Anikeeva, P. O.; Halpert, J. E.; Bawendi, M. G.; Bulović, V. Quantum Dot Light-Emitting Devices with Electroluminescence Tunable over the Entire Visible Spectrum. *Nano Lett.* **2009**, *9*, 2532–2536.
9. He, S.; Li, S.; Wang, F.; Wang, A. Y.; Lin, J.; Tan, Z. Efficient Quantum Dot Light-Emitting Diodes with Solution-Processable Molybdenum Oxide as the Anode Buffer Layer. *Nanotechnology* **2013**, *24*, 175201.
10. Zorn, M.; Bae, W. K.; Kwak, J.; Lee, H.; Lee, C.; Zentel, R.; Char, K. Quantum Dot–Block Copolymer Hybrids with Improved Properties and Their Application to Quantum Dot Light-Emitting Devices. *ACS Nano* **2009**, *3*, 1063–1068.
11. Mankin, M. N.; Mazumder, V.; Sun, S. One-Pot Synthesis of Pt Nanocubes and Nanopods *via* Burst Nucleation and Controlled Secondary Growth. *Chem. Mater.* **2011**, *23*, 132–136.
12. Timonen, J. V. I; Seppälä, E. T.; Ikkala, O.; Ras, R. H. A. From Hot-Injection Synthesis to Heating-Up Synthesis of Cobalt Nanoparticles: Observation of Kinetically Controllable Nucleation. *Angew. Chem.* **2011**, *123*, 2128–2132.
13. Mourdikoudis, S.; Liz-Marzán, L. M. Oleylamine in Nanoparticle Synthesis. *Chem. Mater.* **2013**, *25*, 1465–1476.
14. Xu, S.; Kumar, S.; Nann, T. Rapid Synthesis of High-Quality InP Nanocrystals. *J. Am. Chem. Soc.* **2006**, *128*, 1054–1055.
15. Yin, Y.; Alivisatos, A. P. Colloidal Nanocrystal Synthesis and the Organic–Inorganic Interface. *Nature* **2005**, *437*, 664–670.
16. John, S. S.; Nan, Z.; Hu, N.; Schaefer, D. W.; Angelopoulos, A. P. A Nanoscale-Modified LaMer Model for Particle Synthesis from Inorganic Tin–Platinum Complexes. *J. Mater. Chem.* **2013**, *1*, 8903–8916.

17. Murray, C. B.; Norris, D. J.; Bawendi, M. G. Synthesis and Characterization of Nearly Monodisperse CdE (E = Sulfur, Selenium, Tellurium) Semiconductor Nanocrystallites. *J. Am. Chem. Soc.* **1993**, *115*, 8706–8715.
18. Lin, X. M.; Sorensen, C. M.; Klabunde, K. J. Ligand-Induced Gold Nanocrystal Superlattice Formation in Colloidal Solution. *Chem. Mater.* **1999**, *11*, 198–202.
19. Chan, E. M.; Xu, C.; Mao, A. W.; Han, G.; Owen, J. S.; Cohen, B. E.; Milliron, D. J. Reproducible, High-Throughput Synthesis of Colloidal Nanocrystals for Optimization in Multidimensional Parameter Space. *Nano Lett.* **2010**, *10*, 1874–1885.
20. Dushkin, C.; Saita, S.; Yoshie, K.; Yamaguchi, Y. The Kinetics of Growth of Semiconductor Nanocrystals in a Hot Amphiphile Matrix. *Adv. Colloid Interface Sci.* **2000**, *88*, 37–78.
21. Peng, X.; Wickham, J.; Alivisatos, A. P. Kinetics of II–VI and III–V Colloidal Semiconductor Nanocrystal Growth: "Focusing" of Size Distributions. *J. Am. Chem. Soc.* **1998**, *120*, 5343–5344.
22. LaMer, V. K.; Dinegar, R. H. Theory, Production and Mechanism of Formation of Monodispersed Hydrosols. *J. Am. Chem. Soc.* **1950**, *72*, 4847–4854.
23. Ostwald, W. Uber die vermeintliche Isomerie des roten und gelben Quecksilberoxyds und die Oberflächenspannung. *Z. Phys. Chem.* **1900**, *34*, 495–503.
24. Lifshitz, I. M.; Slyozov, V. V. The Kinetics of Precipitation from Supersaturated Solid Solutions. *J. Phys. Chem. Solids* **1961**, *19*, 35–50.
25. Wagner, C. Theorie der Alterung von Niederschlägen durch Umlösen (Ostwald-Reifung). *Z. Elektrochem.* **1961**, *65*, 581–591.
26. Wey, J. S.; Strong, R. W. Influence of the Gibbs–Thomson Effect on the Growth Behavior of Silver Bromide Crystals. *Photogr. Sci. Eng.* **1977**, *21*, 248–252.
27. Sugimoto, T. Preparation of Monodispersed Colloidal Particles. *Adv. Colloid Interface Sci.* **1987**, *28*, 65–108.
28. Steckel, J. S.; Yen, B. K. H.; Oertel, D. C.; Bawendi, M. G. On the Mechanism of Lead Chalcogenide Nanocrystal Formation. *J. Am. Chem. Soc.* **2006**, *128*, 13032–13033.
29. Owen, J. S.; Chan, E. M.; Liu, H.; Alivisatos, A. P. Precursor Conversion Kinetics and the Nucleation of Cadmium Selenide Nanocrystals. *J. Am. Chem. Soc.* **2010**, *132*, 18206–18213.
30. Allen, P. M.; Walker, B. J.; Bawendi, M. G. Mechanistic Insights into the Formation of InP Quantum Dots. *Angew. Chem., Int. Ed.* **2010**, *49*, 760–762.
31. Joo, J.; Pietryga, J. M.; McGuire, J. A.; Jeon, S.-H.; Williams, D. J.; Wang, H.-L.; Klimov, V. I. A Reduction Pathway in the Synthesis of PbSe Nanocrystal Quantum Dots. *J. Am. Chem. Soc.* **2009**, *131*, 10620–10628.
32. Liu, H.; Owen, J. S.; Alivisatos, A. P. Mechanistic Study of Precursor Evolution in Colloidal Group II–VI Semiconductor Nanocrystal Synthesis. *J. Am. Chem. Soc.* **2007**, *129*, 305–312.
33. Baek, J.; Allen, P. M.; Bawendi, M. G.; Jensen, K. F. Investigation of Indium Phosphide Nanocrystal Synthesis Using a High-Temperature and High-Pressure Continuous Flow Microreactor. *Angew. Chem., Int. Ed.* **2011**, *50*, 627–630.
34. Clark, M. D.; Kumar, S. K.; Owen, J. S.; Chan, E. M. Focusing Nanocrystal Size Distributions *via* Production Control. *Nano Lett.* **2011**, *11*, 1976–1980.
35. Dagtepe, P.; Chikan, V. Quantized Ostwald Ripening of Colloidal Nanoparticles. *J. Phys. Chem. C* **2010**, *114*, 16263–16269.
36. Johnson, N. J. J.; Korinek, A.; Dong, C.; van Veggel, F. C. J. M. Self-Focusing by Ostwald Ripening: A Strategy for Layer-by-Layer Epitaxial Growth on Upconverting Nanocrystals. *J. Am. Chem. Soc.* **2012**, *134*, 11068–11071.
37. Washington, A. L.; Foley, M. E.; Cheong, S.; Quffa, L.; Breshike, C. J.; Watt, J.; Tilley, R. D.; Strouse, G. F. Ostwald's Rule of Stages and Its Role in CdSe Quantum Dot Crystallization. *J. Am. Chem. Soc.* **2012**, *134*, 17046–17052.
38. Bawendi, M. G.; Kortan, A. R.; Steigerwald, M. L.; Brus, L. E. X-ray Structural Characterization of Larger CdSe Semiconductor Clusters. *J. Chem. Phys.* **1989**, *91*, 7282–7290.
39. Wang, Y.; Zhang, L.; Deng, K.; Chen, X.; Zou, Z. Low Temperature Synthesis and Photocatalytic Activity of Rutile TiO_2 Nanorod Superstructures. *J. Phys. Chem. C* **2007**, *111*, 2709–2714.
40. Ostwald, W. Studien über die Bildung und Umwandlung fester Körper. 1. Abhandlung: Ubersättigung und Uberkaltung. *Z. Phys. Chem.* **1897**, *22*, 289–330.
41. Haase, M.; Schäfer, H. Upconverting Nanoparticles. *Angew. Chem., Int. Ed.* **2011**, *50*, 5808–5829.
42. Haase, M.; Schäfer, H. Nanopartikel für die Aufwärtskonversion. *Angew. Chem.* **2011**, *123*, 5928–5950.
43. Johnson, N. J. J.; Oakden, W.; Stanisz, G. J.; Scott Prosser, R.; van Veggel, F. C. J. M. Size-Tunable, Ultrasmall $NaGdF_4$ Nanoparticles: Insights into Their T_1 MRI Contrast Enhancement. *Chem. Mater.* **2011**, *23*, 3714–3722.
44. Das, G. K.; Johnson, N. J. J.; Cramen, J.; Blasiak, B.; Latta, P.; Tomanek, B.; van Veggel, F. C. J. M. $NaDyF_4$ Nanoparticles as T_2 Contrast Agents for Ultrahigh Field Magnetic Resonance Imaging. *J. Phys. Chem. Lett.* **2012**, *3*, 524–529.
45. Cheng, L.; Wang, C.; Liu, Z. Upconversion Nanoparticles and Their Composite Nanostructures for Biomedical Imaging and Cancer Therapy. *Nanoscale* **2013**, *5*, 23–37.
46. Wang, M.; Abbineni, G.; Clevenger, A.; Mao, C.; Xu, S. Upconversion Nanoparticles: Synthesis, Surface Modification and Biological Applications. *Nanomed. Nanotechnol. Biol. Med.* **2011**, *7*, 710–729.
47. Mai, H.-X.; Zhang, Y.-W.; Si, R.; Yan, Z.-G.; Sun, L.; You, L.-P.; Yan, C.-H. High-Quality Sodium Rare-Earth Fluoride Nanocrystals: Controlled Synthesis and Optical Properties. *J. Am. Chem. Soc.* **2006**, *128*, 6426–6436.
48. Mai, H.-X.; Zhang, Y.-W.; Sun, L.-D.; Yan, C.-H. Highly Efficient Multicolor Up-conversion Emissions and Their Mechanisms of Monodisperse $NaYF_4$:Yb,Er Core and Core/Shell-Structured Nanocrystals. *J. Phys. Chem. C* **2007**, *111*, 13721–13729.
49. Rahman, P.; Green, M. The Synthesis of Rare Earth Fluoride Based Nanoparticles. *Nanoscale* **2009**, *1*, 214–224.
50. Li, X.; Gai, S.; Li, C.; Wang, D.; Niu, N.; He, F.; Yang, P. Monodisperse Lanthanide Fluoride Nanocrystals: Synthesis and Luminescent Properties. *Inorg. Chem.* **2012**, *51*, 3963–3971.
51. Zheng, T.; Sun, L.-D.; Zhou, J.-C.; Feng, W.; Zhang, C.; Yan, C.-H. Construction of $NaREF_4$-Based Binary and Bilayer Nanocrystal Assemblies. *Chem. Commun.* **2013**, *49*, 5799–5801.
52. Mai, H.-X.; Zhang, Y.-W.; Sun, L.-D.; Yan, C.-H. Orderly Aligned and Highly Luminescent Monodisperse Rare-Earth Orthophosphate Nanocrystals Synthesized by a Limited Anion-Exchange Reaction. *Chem. Mater.* **2007**, *19*, 4514–4522.
53. Mai, H.-X.; Zhang, Y.-W.; Sun, L.-D.; Yan, C.-H. Size- and Phase-Controlled Synthesis of Monodisperse $NaYF_4$:Yb,Er Nanocrystals from a Unique Delayed Nucleation Pathway Monitored with Upconversion Spectroscopy. *J. Phys. Chem. C* **2007**, *111*, 13730–13739.
54. Komban, R.; Klare, J. P.; Voss, B.; Nordmann, J.; Steinhoff, H.-J.; Haase, M. An Electron Paramagnetic Resonance Spectroscopic Investigation on the Growth Mechanism of $NaYF_4$:Gd Nanocrystals. *Angew. Chem., Int. Ed.* **2012**, *51*, 6506–6510.
55. Komban, R.; Klare, J. P.; Voss, B.; Nordmann, J.; Steinhoff, H.-J.; Haase, M. Elektronenspinresonanz-Untersuchungen zum Wachstumsmechanismus von $NaYF_4$:Gd-Nanokristallen. *Angew. Chem.* **2012**, *124*, 6612–6616.
56. Voß, B.; Nordmann, J.; Uhl, A.; Komban, R.; Haase, M. Effect of the Crystal Structure of Small Precursor Particles on the Growth of β-$NaREF_4$ (RE = Sm, Eu, Gd, Tb) Nanocrystals. *Nanoscale* **2012**, *5*, 806–812.
57. Shan, J.; Qin, X.; Yao, N.; Ju, Y. Synthesis of Monodisperse Hexagonal $NaYF_4$:Yb, Ln (Ln = Er, Ho and Tm) Upconversion Nanocrystals in TOPO. *Nanotechnology* **2007**, *18*, 445607.
58. Boyer, J.-C.; Vetrone, F.; Cuccia, L. A.; Capobianco, J. A. Synthesis of Colloidal Upconverting $NaYF_4$ Nanocrystals Doped with Er^{3+}, Yb^{3+} and Tm^{3+}, Yb^{3+} *via* Thermal

Decomposition of Lanthanide Trifluoroacetate Precursors. *J. Am. Chem. Soc.* **2006**, *128*, 7444–7445.
59. Shan, J.; Yao, N.; Ju, Y. Phase Transition Induced Formation of Hollow Structures in Colloidal Lanthanide-Doped $NaYF_4$ Nanocrystals. *J. Nanopart. Res.* **2009**, *12*, 1429–1438.
60. Talapin, D. V.; Rogach, A. L.; Haase, M.; Weller, H. Evolution of an Ensemble of Nanoparticles in a Colloidal Solution: Theoretical Study. *J. Phys. Chem. B* **2001**, *105*, 12278–12285.
61. Mersmann, A. Calculation of Interfacial Tensions. *J. Cryst. Growth* **1990**, *102*, 841–847.
62. Lide, D. R. *CRC Handbook of Chemistry & Physics*, 74th ed.; CRC Press: Boca Raton, FL, 1993.
63. Rempel, J. Y.; Bawendi, M. G.; Jensen, K. F. Insights into the Kinetics of Semiconductor Nanocrystal Nucleation and Growth. *J. Am. Chem. Soc.* **2009**, *131*, 4479–4489.
64. Mantzaris, N. V. Liquid-Phase Synthesis of Nanoparticles: Particle Size Distribution Dynamics and Control. *Chem. Eng. Sci.* **2005**, *60*, 4749–4770.
65. van Embden, J.; Sader, J. E.; Davidson, M.; Mulvaney, P. Evolution of Colloidal Nanocrystals: Theory and Modeling of Their Nucleation and Growth. *J. Phys. Chem. C* **2009**, *113*, 16342–16355.
66. Thoma, R. E.; Insley, H.; Hebert, G. M. The Sodium Fluoride-Lanthanide Trifluoride Systems. *Inorg. Chem.* **1966**, *5*, 1222–1229.
67. Liu, C.; Wang, H.; Zhang, X.; Chen, D. Morphology- and Phase-Controlled Synthesis of Monodisperse Lanthanide-Doped $NaGdF_4$ Nanocrystals with Multicolor Photoluminescence. *J. Mater. Chem.* **2009**, *19*, 489.
68. Mullin, J. W. Nucleation. *Crystallization*; Butterworth-Heinemann: Boston, MA, 2001; pp 182−189.
69. Navrotsky, A. Energetics of Nanoparticle Oxides: Interplay between Surface Energy and Polymorphism. *Geochem. Trans.* **2003**, *4*, 34.
70. Hoffman, J. D. Thermodynamic Driving Force in Nucleation and Growth Processes. *J. Chem. Phys.* **1958**, *29*, 1192.
71. Park, J.; An, K.; Hwang, Y.; Park, J. G.; Noh, H. J.; Kim, J. Y.; Park, J. H.; Hwang, N. M.; Hyeon, T. Ultra-Large-Scale Syntheses of Monodisperse Nanocrystals. *Nat. Mater.* **2004**, *3*, 891–895.
72. Schneider, C. A.; Rasband, W. S.; Eliceiri, K. W. NIH Image to ImageJ: 25 Years of Image Analysis. *Nat. Methods* **2012**, *9*, 671–675.
73. Rodríguez-Carvajal, J. Recent Advances in Magnetic Structure Determination by Neutron Powder Diffraction. *Physica B* **1993**, *192*, 55–69.